Mathematical Biosciences 295 (2018) 11–23

Contents lists available at ScienceDirect

Mathematical Biosciences

journal homepage: www.elsevier.com/locate/mbs

A numerical framework for drug transport in a multi-layer system with discontinuous interlayer condition

Kristinn Gudnason*[,a], Sven Sigurdsson[a], Bergthora S. Snorradottir[b], Mar Masson[b], Fjola Jonsdottir[a]

[a] Faculty of Industrial Engineering, Mechanical Engineering and Computer Science, University of Iceland, Iceland
[b] Faculty of Pharmaceutical Science, University of Iceland, Iceland

ARTICLE INFO

Keywords:
Discontinuous boundary conditions
Targeted drug delivery
Controlled release

ABSTRACT

Discontinuous boundary conditions arise naturally when describing various physical phenomena and numerically modelling such conditions can prove difficult. In the field of pharmaceutical sciences, two such cases are the partitioning of a compound between different materials and a flux rate membrane controlling mass transfer between materials which both result in a discontinuous jump in concentration across adjacent materials. In this study, we introduce a general one-dimensional finite element drug delivery framework, which along with diffusion, reversible binding and dissolution within material layers, incorporates the partitioning and mass transfer conditions between layers of material.

We apply the framework to construct models of experiments, which along with experimental data, allow us to infer pharmacokinetic properties of potential material for drug delivery. Understanding such material properties is the key to optimising the therepeutic effect of a targeted drug delivery system.

1. Introduction

For the treatment of localized diseases, therapuetic levels of medication need to be sustained in areas which can be hard to reach. Effective optimization techniques for targeted drug delivery require understanding of the various pharmacokinetic processes involved. Mathematical models that accurately describe these processes are a valuable tool in the estimation of the properties of potential drug carrying materials, which can subsequently be used to forecast the distribution within specific regions of the body during delivery.

In this paper, a numerical framework that incorporates the physical processes required to simulate various drug delivery systems is introduced. The framework presented is a one-dimensional, multi-layer model that is governed primarily by a diffusion-reaction equation, but also allows for two types of coupled secondary state, chosen independently within each layer. The secondary state is governed by either the Noyes–Whitney equation, as presented by Frenning et al. [1,2], or the two-phase mathematical model presented by Pontrelli and de Monte [3], for transdermal drug delivery. Our numerical model can be applied to the modelling of drug release from a delivery device to the target area with dissolution, absorption, and reversible binding taking place in any of various layers involved, both in the delivery device and target system.

One of the challenging aspects of numerical modeling in this context is accurately considering the interface conditions and the associated discontinuities in drug concentration that stem from both partitioning and interfacial resistance or surface barriers. This is a challenging subject that has been considered in the past by e.g. Hickson et al. [4] and Rim et al. [5]. Rim et al. constructed a finite element model for transdermal drug delivery, incorporating the effects of partitioning between layers. Their approach is based on decomposing a partition interface into two adjacent boundaries belonging to separate layers. A mixed method is employed, whereby cross boundary normal flux and concentrations at each boundary are modeled as independent variables. McGinty and Pontrelli [6] recently presented a drug release-absorption model based on finite differences that deals with discontinuities in concentration caused by interlayer mass transfer conditions which describe interfacial resistance. Their model is based on a special difference scheme developed by Hickson et al. [4]. The models developed by Hickson et al. and Rim et al. both contain a concentration discontinuity condition across the boundary. Gupta et al. [7] introduced a model characterizing transport of a lipophilic solute across the cornea with good comparisson with trans-corneal concentration profiles from experiments. Results exhibit the importance of incorporating the effects of partitioning and interfacial resistance between the epithelium, stroma and endothelium layers as well as at outer boundaries. Pimenta et al.

* Corresponding author.
E-mail address: krg13@hi.is (K. Gudnason).

http://dx.doi.org/10.1016/j.mbs.2017.10.012
Received 15 April 2017; Received in revised form 30 September 2017; Accepted 20 October 2017
Available online 26 October 2017

[8] successfully determined the partition coefficient of poly-hydroxyethylmethacrylate and silicone based hydrogels in combination with three different drugs.

The work presented in this paper incorporates all the boundary effects mentioned above, including partitioning, mass transfer effects and flux continuity, into a finite element formulation that eliminates the need for additional variables or special schemes at the boundaries. The approach is based on a two step construction. First, the finite element scheme is constructed separately for each layer with arbitrary flux conditions at the outer boundaries of each one. Following that, the layer equations are assembled into a global scheme that ensures continuous flux between layers while at the same time satisfying the interlayer boundary conditions.

The capabilities of the numerical framework presented are demonstrated, and the importance of incorporating both partitioning and mass transfer effects is highlighted by constructing models describing different aspects of drug transport. The numerical framework is used to simulate three cases. First, we simulate an moxifloxacin impregnated intra-ocular lense in a Franz diffusion cell with three different thicknesses of lens material. The results are compared with experimental data. The second case models a two phase transdermal system developed by Pontrelli and de Monte [3]. The third case is a reevaluation of data presented in Snorradottir et al. [9], on transdermal drug delivery. Results show the importance of having interlayer conditions that include both partition and mass transfer effects and that the proposed framework can apply successfully to all the cases considered.

2. Model

The mathematical model presented below consists of two coupled partial differential equations, describing possible drug related physical processes taking place within a sequence of layers of different materials, along with general boundary conditions capturing possible cross layer mechanisms. The model is one-dimensional with respect to space.

2.1. Layer equations

Within a given layer α, of thickness H_α, demarked by points $x_{\alpha-1}$ and x_α, we model two variables, an unbound fluid state C_α and a bound secondary state S_α in terms of concentration (mg/cm^3), with the following set of coupled partial differential equations

$$\begin{aligned}\frac{\partial C_\alpha(x,t)}{\partial t} &= \frac{\partial}{\partial x}\left(D_\alpha \frac{\partial C_\alpha(x,t)}{\partial x}\right) - d_\alpha C_\alpha(x,t) - b_\alpha(S_\alpha(x,t), C_\alpha(x,t))\\ \frac{\partial S_\alpha(x,t)}{\partial t} &= b_\alpha(S_\alpha(x,t), C_\alpha(x,t))\end{aligned} \tag{1}$$

where D_α is the diffusion coefficient (cm^2/h), d_α is a decay coefficient within the layer, which may e.g. describe leakage or metabolic consumption (1/h). The term $b_\alpha(S_\alpha(x,t), C_\alpha(x,t))$ relates the binding and unbinding process. We use schematic diagrams, such as the one depicted in Fig. 1, to vizualize models. In order to describe the release from solid drug systems we let S_α signify the solid state and choose the Noyes–Whitney equation [10] to describe dissolution

$$b_\alpha(S_\alpha(x,t), C_\alpha(x,t)) = -A_{0,\alpha}k_\alpha\left(\frac{S_\alpha(x,t)}{S_\alpha(x,0)}\right)^{2/3}(c_{s,\alpha} - C_\alpha(x,t)) \tag{2}$$

where $k_{d,\alpha}$ is the dissolution rate coefficient of solid drug (cm/h), $c_{s,\alpha}$ is the solubility of the drug (mg/cm^3), $A_{0,\alpha}$ is the initial surface area of the solid drug per unit volume (cm^2/cm^3), where the drug particles are assumed implicitly by the model to retain their shape as the drug dissolves such that the surface area is proportional to the volume to the power of 2/3 [11]. Initial concentrations of bound drug $S_\alpha(x,0)$ and unbound drug $C_\alpha(x,0)$ must be specified in each layer. Expression (2) can be made linear with respect to the secondary state variable by introducing a new dependent variable $\widehat{S}_\alpha(x,t) = S_\alpha^{1/3}(x,t)$ as is done in [9]. Then (1) becomes

$$\begin{aligned}\frac{\partial C_\alpha(x,t)}{\partial t} &= \frac{\partial}{\partial x}\left(D_\alpha \frac{\partial C_\alpha(x,t)}{\partial x}\right) - d_\alpha C_\alpha(x,t)\\ &\quad + k'_\alpha \widehat{S}_\alpha(x,0)\widehat{S}_\alpha^2(x,t)(c_{s,\alpha} - C_\alpha(x,t))\\ \frac{\partial \widehat{S}_\alpha(x,t)}{\partial t} &= -\frac{k'_\alpha}{3}\widehat{S}_\alpha(x,0)(c_{s,\alpha} - C_\alpha(x,t))\end{aligned} \tag{3}$$

where $k'_\alpha = k_\alpha A_{0,\alpha}/S_\alpha(x,0)$ is the effective dissolution rate (cm^3/[mg h]). The presentation of the finite element approximation and the time stepping procedure in this paper is based on the assumption that the secondary state equation is linear with respect to the secondary state variable, as well as the primary state equation being linear with respect to the primary state variable. Note that Eq. (3) and the modification after Eq. (4) both satisfy this assumption. The binding and unbinding process can be in the form of a two-phase equation

$$b_\alpha(S_\alpha(x,t), C_\alpha(x,t)) = -k_1 S_\alpha(x,t) + k_2 C_\alpha(x,t) \tag{4}$$

where k_1 and k_2 are unbinding and binding rate coefficients (1/h), respectively. In some applications it is appropriate to assume a conservation condition for binding by replacing the k_2 coefficient with $k'_2(S_{max,\alpha} - S_\alpha(x,t))$, where $S_{max,\alpha}$ denotes the density of binding sites [6]. In this case the model is non-linear and the present finite element method has to be modified by linearizing the equation in an appropriate way.

2.2. General boundary conditions

Between layers we define general interlayer boundary conditions with which we are able to describe the combined mechanisms of partitioning and mass transfer rate.

A partition between layers, occuring at x_α, describes a concentration discontinuity in equilibrium determined by the ratio P_α, refered to as the partition coefficient (dimensionless). The ratio controls the jump in concentration on one side of an interface proportionally with respect to the concentration of the other side. The mass transfer coefficient K_α (cm/h) controls the flux resistance across the interface possibly due to a thin diffusion barrier. For interlayer boundary point x_α, we have

$$\begin{aligned}&-D_\alpha \frac{\partial C_\alpha}{\partial x}\bigg|_{x=x_\alpha^-} = -D_{\alpha+1}\frac{\partial C_{\alpha+1}}{\partial x}\bigg|_{x=x_\alpha^+}\\ &= K_\alpha(C_\alpha(x_\alpha,t) - P_\alpha C_{\alpha+1}(x_\alpha,t))\end{aligned} \tag{5}$$

Low K_α slows the rate at which the ratio of concentration difference between the layers approaches the ratio P_α. Sometimes it may be more appropriate to express the right-hand side of (5) as

$$K'_\alpha(P'_\alpha C_\alpha(x_\alpha,t) - C_{\alpha+1}(x_\alpha,t))$$

This can be realised by setting $K_\alpha = K'_\alpha P'_\alpha$ and $P_\alpha = 1/P'_\alpha$. When needed we shall refer to K and P as the layer α / layer $\alpha+1$ mass transfer and partition coefficients respectively and refer to K' and P' as the layer $\alpha+1$ / layer α mass transfer and partition coefficients. For simplicity, we may refer to the flux at x_α as J_α. Alternatively, we can express (5) as

$$K_{\alpha-}C_\alpha(x_\alpha,t) - K_{\alpha+}C_{\alpha+1}(x_\alpha,t) \tag{6}$$

and refer to $K_{\alpha-} = K_\alpha$ and $K_{\alpha+} = K_\alpha P_\alpha = K'_\alpha$ as the left and right rate coefficients at $x = x_\alpha$, cf. (4). At outer boundaries x_0 and x_N we define general outer boundary conditions in a similar manner

$$\begin{aligned}-D_1\frac{\partial C_1(x,t)}{\partial x}\bigg|_{x=x_0} &= K_0(C_{b,0} - P_0 C_1(x_0,t))\\ -D_N\frac{\partial C_N(x,t)}{\partial x}\bigg|_{x=x_N} &= K_N(C_N(x_N,t) - P_N C_{b,N})\end{aligned} \tag{7}$$

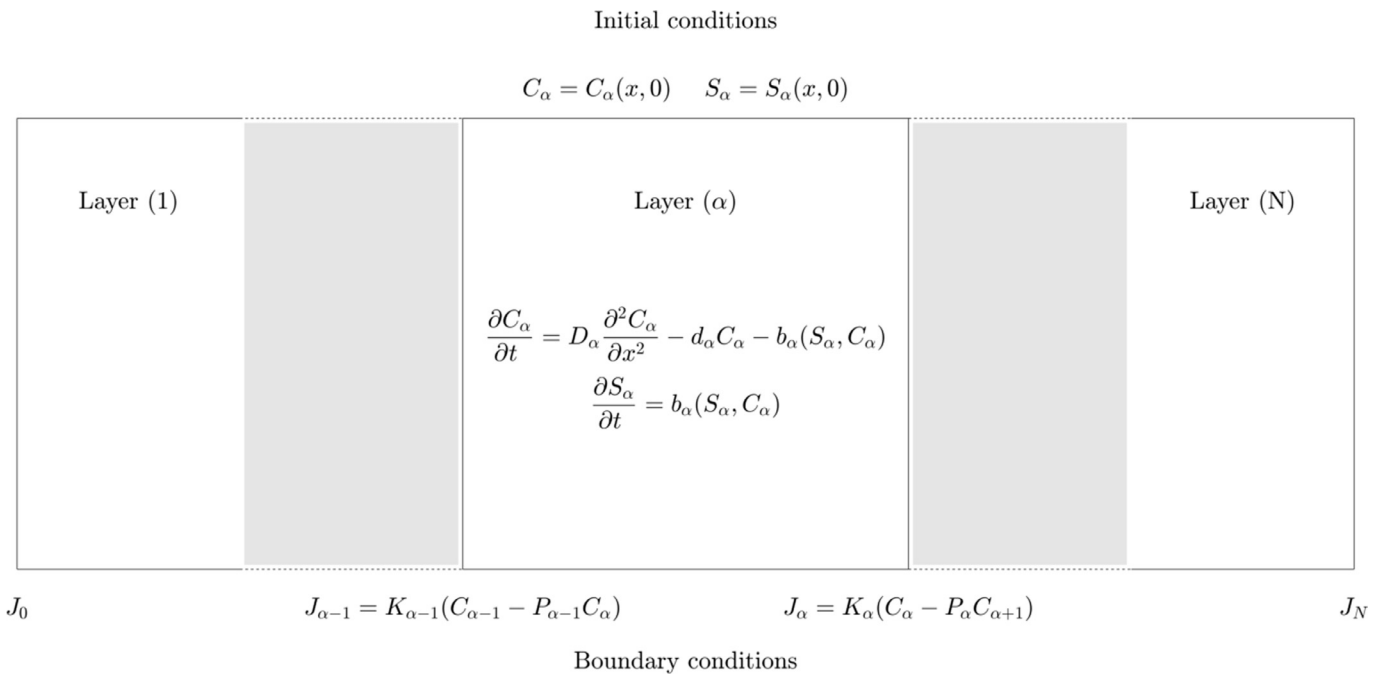

Fig. 1. A schematic model showing diffusion and decay, coupled with secondary state within layer α. General boundary conditions are shown at interlayer boundaries.

where $C_{b,0}$ and $C_{b,N}$ are specified concentration values outside the first and last layer, respectively. These general conditions can be reduced to the following special cases:

(a) Kedem–Katchalsky condition

By setting $P_\alpha = 1$, in (5), the general boundary condition reduces to the Kedem–Katchalsky condition

$$-D_\alpha \frac{\partial C_\alpha}{\partial x}\bigg|_{x=x_\alpha^-} = -D_{\alpha+1}\frac{\partial C_{\alpha+1}}{\partial x}\bigg|_{x=x_\alpha^+} = K_\alpha(C_\alpha(x_\alpha, t) - C_{\alpha+1}(x_\alpha, t))$$

which can also be interpreted as the left and right rate coefficients in (6) being the same. It can be used to describe a thin rate controlling barrier with thickness h and diffusion coefficient D where $D/h \to K_\alpha$ as $h \to 0$.

(b) Partitioning condition

Note by dividing (5) by K_α and setting $K_\alpha \to \infty$ that we have

$$\frac{D_\alpha}{K_\alpha}\frac{\partial C_\alpha}{\partial x}\bigg|_{x=x_\alpha^-} = \frac{D_{\alpha+1}}{K_\alpha}\frac{\partial C_{\alpha+1}}{\partial x}\bigg|_{x=x_\alpha^+} \longrightarrow 0$$

and so setting K_α 'high' effectively reduces the boundary condition to the partitioning condition

$$C_\alpha(x_\alpha, t) - P_\alpha C_{\alpha+1}(x_\alpha, t) = 0$$

which can also be interpreted as having differing rate coefficients in (6) and the flux being negligible in comparison.

(c) Control barrier with partition

Assume that we have a thin controlling barrier layer with thickness h and diffusion parameter D, inserted between layers α and $\alpha+1$, and that the partition coefficients, between layer α and the barrier and between the barrier and layer $\alpha+1$, are P_- and P_+, respectively. Likewise, we signify concentration at the different sides of the barrier to be C_- and C_+, respectively. Assuming a constant spatial concentration gradient through the barrier, we have $C_- = P_-^{-1}C_\alpha(x_\alpha, t)$ and $C_+ = P_+C_{\alpha+1}(x_\alpha, t)$, and the concentration profile through the barrier is linear. This leads to the following expression for the flux through the barrier

$$-D\frac{C_+ - C_-}{h} = -D\frac{P_+C_{\alpha+1}(x_\alpha, t) - P_-^{-1}C_\alpha(x_\alpha, t)}{h}$$

and thus as $h \to 0$ the effect of the barrier reduces to condition (5) with $K_\alpha = \frac{D}{hP_-}$ and $P_\alpha = P_-P_+$.

Note that continuous concentration across an interlayer boundary can be achieved by setting $P_\alpha = 1$ and setting K_α 'high' as was done to evoke the partitioning condition so that $C_\alpha(x_\alpha, t) - C_{\alpha+1}(x_\alpha, t) \approx 0$. Also note, that by setting $K_\alpha = 0$, an impermeable concentration barrier is created resulting in $J_\alpha = 0$.

2.3. Finite element formulation

We now describe how we numerically approximate the mathematical model outlined above. The discretization approach is based on a two step contruction. First, the finite element scheme is constructed separately for each layer with arbitrary flux conditions at the outer boundaries of each one. Following that, the layer equations are assembled into a global scheme that ensures continuous flow between layers while at the same time satisfying the interlayer boundary conditions.

Discretization within layers

Over a given interval $I_j = [x_j, x_{j+1}]$, contained within layer α, with $j = 0, 1, \cdots, n_\alpha - 1$, we have the weak formulation of the primary phase

$$\begin{aligned}\int_{I_j} \frac{\partial C_\alpha}{\partial t} w\, dx = &- \int_{I_j} D_\alpha \frac{\partial C_\alpha}{\partial x}\frac{\partial w}{\partial x}\, dx + f_{\alpha,x_j}\, w(x_j) - f_{\alpha,x_{j+1}}\, w(x_{j+1}) \\ &- \int_{I_j} d_\alpha C_\alpha w\, dx - \int_{I_j} b_\alpha(S_\alpha, C_\alpha)\, w\, dx\end{aligned} \tag{8}$$

where w denotes a test function and the x-directional flux at x_k is defined as

$$f_{\alpha,x_k} = -D_\alpha \frac{\partial C_\alpha}{\partial x}\bigg|_{x=x_k}$$

which we will get back to later. Here n_α is the number of intervals within layer α and we shall assume that they are all of the same length $h_\alpha = H_\alpha/n_\alpha$, i.e. $|I_j| = h_\alpha$ for all j.

In order to obtain a linear approximation over interval I_j, we define

linear nodal basis functions φ_j and φ_{j+1} at x_j and x_{j+1} respectively, such that φ_j and φ_{j+1} take the value 1 at x_j and x_{j+1} respectively and the value 0 at the opposite node. Thus we may approximate $C_\alpha(x,\, t)$ and $S_\alpha(x,\, t)$ over I_j with $\widehat{C}_\alpha(x,\, t)$ and $\widehat{S}_\alpha(x,\, t)$

$$\widehat{C}_\alpha(x,\, t) = c_{\alpha,j}(t)\varphi_j(x) + c_{\alpha,j+1}(t)\varphi_{j+1}(x)$$
$$\widehat{S}_\alpha(x,\, t) = s_{\alpha,j}(t)\varphi_j(x) + s_{\alpha,j+1}(t)\varphi_{j+1}(x)$$

where $c_{\alpha,\,j}(t)$ and $s_{\alpha,\,j}(t)$ are time dependant coefficients of primary and secondary phases amounting to the approximate values for C_α and S_α at $x = x_j$.

Now let $\boldsymbol{M}_\alpha$ denote the local mass matrix, $\overline{\boldsymbol{M}}_\alpha$ the lumped form approximation thereof and $\boldsymbol{K}_\alpha$ denote the local stiffness matrix. For a linear approximation we have that

$$\boldsymbol{M}_\alpha = \frac{h_\alpha}{6}\begin{bmatrix} 2 & 1 \\ 1 & 2 \end{bmatrix} \qquad \overline{\boldsymbol{M}}_\alpha = \frac{h_\alpha}{2}\begin{bmatrix} 1 & 0 \\ 0 & 1 \end{bmatrix} \qquad \boldsymbol{K}_\alpha = \frac{1}{h_\alpha}\begin{bmatrix} 1 & -1 \\ -1 & 1 \end{bmatrix}$$

where h_α is the length of I_j. First we discretize the left hand side of (8)

$$\int_{I_j} \frac{\partial \widehat{C}_\alpha}{\partial t}\varphi_i \, dx\bigg|_{i=j,j+1} = \boldsymbol{M}_\alpha \frac{d}{dt}\begin{bmatrix} c_{\alpha,j} \\ c_{\alpha,j+1} \end{bmatrix} \approx \overline{\boldsymbol{M}}_\alpha \frac{d}{dt}\begin{bmatrix} c_{\alpha,j} \\ c_{\alpha,j+1} \end{bmatrix} \tag{9}$$

Discretizing the terms depending only on C_α on the right hand side of (8), we get

$$\left(-\int_{I_j} D_\alpha \frac{\partial \widehat{C}_\alpha}{\partial x}\frac{\partial \varphi_i}{\partial x}\, dx - \int_{I_j} d_\alpha \widehat{C}_\alpha \varphi_i \, dx\right)\bigg|_{i=j,j+1} = -(D_\alpha \boldsymbol{K}_\alpha + d_\alpha \boldsymbol{M}_\alpha)\begin{bmatrix} c_{\alpha,j} \\ c_{\alpha,j+1} \end{bmatrix}$$

We next note that

$$f_{\alpha,j}\ \varphi_i - f_{\alpha,j+1}\ \varphi_i = \begin{cases} f_{\alpha,j} & i = j \\ -f_{\alpha,j+1} & i = j+1 \end{cases}$$

Finally, in the two-phase case we discretize the last term of (8) as

$$\int_{I_j} (-k_1 \widehat{S}_\alpha \varphi_i + k_2 \widehat{C}_\alpha \varphi_i)\, dx\bigg|_{i=j,j+1} = -k_1 \boldsymbol{M}_\alpha \begin{bmatrix} s_{\alpha,j} \\ s_{\alpha,j+1} \end{bmatrix} + k_2 \boldsymbol{M}_\alpha \begin{bmatrix} c_{\alpha,j} \\ c_{\alpha,j+1} \end{bmatrix} \tag{10}$$

The procedure for the Noyes–Whitney equation is similar after using the transformed Eqs. (3). Note that in the equation for the primary phase we treat $\widehat{S}_\alpha^2(x,\, t)$ as a given value along with c_s and in the equation for the secondary phase we treat $C_\alpha(x,\, t)$ as given. Introducing the notation

$$\boldsymbol{C}_L = (-D_\alpha \boldsymbol{K}_\alpha - (d_\alpha + k_1)\overline{\boldsymbol{M}}_\alpha) \qquad \boldsymbol{S}_L = k_2 \overline{\boldsymbol{M}}_\alpha$$

we are now ready to express the discretisation over I_j in the two phase case in matrix vector form as

$$\overline{\boldsymbol{M}}_\alpha \frac{d}{dt}\begin{bmatrix} c_{\alpha,j} \\ c_{\alpha,j+1} \end{bmatrix} = \boldsymbol{C}_L \begin{bmatrix} c_{\alpha,j} \\ c_{\alpha,j+1} \end{bmatrix} + \boldsymbol{S}_L \begin{bmatrix} s_{\alpha,j} \\ s_{\alpha,j+1} \end{bmatrix} + \begin{bmatrix} f_{\alpha,j} \\ -f_{\alpha,j+1} \end{bmatrix} \tag{11}$$

For now, we treat the secondary state variables as given as we develop a formulation with which we will update the primary state variables. Assembling contributions over all I_j leads to the discrete approximation for layer α, expressed as a matrix equation of the following form:

$$\frac{h_\alpha}{2}\frac{d}{dt}\begin{bmatrix} c_{\alpha,0} \\ 2c_{\alpha,1} \\ \vdots \\ 2c_{\alpha,n_\alpha-1} \\ c_{\alpha,n_\alpha} \end{bmatrix} = \begin{bmatrix} \boldsymbol{x} & \boldsymbol{x} & & & \\ \boldsymbol{x} & \boldsymbol{xx} & \boldsymbol{x} & & \\ & \ddots & \ddots & \ddots & \\ & & \boldsymbol{x} & \boldsymbol{xx} & \boldsymbol{x} \\ & & & \boldsymbol{x} & \boldsymbol{x} \end{bmatrix}\begin{bmatrix} c_{\alpha,0} \\ c_{\alpha,1} \\ \vdots \\ c_{\alpha,n_\alpha-1} \\ c_{\alpha,n_\alpha} \end{bmatrix} + \begin{bmatrix} \boldsymbol{y} - f_{\alpha,0} \\ \boldsymbol{y} \\ \vdots \\ \boldsymbol{y} \\ \boldsymbol{y} + f_{\alpha,n_\alpha} \end{bmatrix}$$

where local matrix $\boldsymbol{C_L}$ contributes to the tridiagonal matrix, signified by $\boldsymbol{x}$, and the local matrix $\boldsymbol{S_L}$ contributes to the load vector, signified by $\boldsymbol{y}$. Along with $\boldsymbol{y}$, the interlayer flux $f_{\alpha,0}$ and f_{α,n_α}, which we get from (5), contribute to the load vector

$$f_{\alpha,0} = K_{\alpha-1}\left(u_{\alpha-1,n_{\alpha-1}} - P_{\alpha-1}u_{\alpha,0}\right)$$
$$f_{\alpha,n_\alpha} = K_\alpha\left(u_{\alpha,n_\alpha} - P_\alpha u_{\alpha+1,0}\right)$$

whereas all interelement fluxes cancel out by flux continuity. In the case of the first and last layers, $f_{1,0}$ and f_{N,n_N}, respectively, have to be specified by the given outer boundary conditions (7).

Global assembly

To create a global system of equations, we need to assemble the layer systems. This involves inserting the interlayer flux from the load vectors into the global matrix. In the case of the interface between layers α and $\alpha + 1$ we have fluxes f_{α,n_α} and $f_{\alpha+1,0}$ noting that the distinct variables, c_{α,n_α} and $c_{\alpha+1,0}$, are the approximations for $C_\alpha(x_\alpha^-,\, t)$ and $C_\alpha(x_\alpha^+,\, t)$ respectively.

$$\begin{matrix} \frac{h_\alpha}{2}\frac{d}{dt}\begin{bmatrix} \vdots \\ 2c_{\alpha,n_\alpha-1} \\ c_{\alpha,n_\alpha} \end{bmatrix} \\ \frac{h_{\alpha+1}}{2}\frac{d}{dt}\begin{bmatrix} c_{\alpha+1,0} \\ 2c_{\alpha+1,1} \\ \vdots \end{bmatrix} \end{matrix} = \begin{vmatrix} \ddots & \ddots & \ddots & & \\ & \boldsymbol{x} & \boldsymbol{xx} & \boldsymbol{x} & \\ & & \boldsymbol{x} & \boldsymbol{x}+K_\alpha & -K_\alpha P_\alpha \\ & & & -K_\alpha P_\alpha & \begin{bmatrix} \boldsymbol{x}+K_\alpha P_\alpha & \boldsymbol{x} & \\ \boldsymbol{x} & \boldsymbol{xx} & \boldsymbol{x} \\ & \ddots & \ddots & \ddots \end{bmatrix} \end{vmatrix} \begin{vmatrix} \vdots \\ c_{\alpha,n_\alpha-1} \\ c_{\alpha,n_\alpha} \\ c_{\alpha+1,0} \\ c_{\alpha+1,1} \\ \vdots \end{vmatrix} + \begin{vmatrix} \vdots \\ \boldsymbol{y} \\ \boldsymbol{y} \\ \boldsymbol{y} \\ \boldsymbol{y} \\ \vdots \end{vmatrix}$$

This leaves all flux contributions to the load vector empty except for the top

$$\frac{h_1}{2}\frac{d}{dt}\begin{bmatrix} c_{1,0} \\ 2c_{1,1} \\ \vdots \end{bmatrix} = \begin{bmatrix} \boldsymbol{x}+K_0P_0 & \boldsymbol{x} & \\ \boldsymbol{x} & \boldsymbol{xx} & \boldsymbol{x} \\ & \ddots & \ddots & \ddots \end{bmatrix}\begin{bmatrix} c_{1,0} \\ c_{1,1} \\ \vdots \end{bmatrix} - \begin{bmatrix} \boldsymbol{y}+K_0C_{b,0} \\ \boldsymbol{y} \\ \vdots \end{bmatrix}$$

and the bottom

$$\frac{h_N}{2}\frac{d}{dt}\begin{bmatrix} \vdots \\ 2c_{N,n_N-1} \\ c_{N,n_N} \end{bmatrix} = \begin{bmatrix} \ddots & \ddots & \ddots & \\ & \boldsymbol{x} & \boldsymbol{xx} & \boldsymbol{x} \\ & & \boldsymbol{x} & \boldsymbol{x}+K_N \end{bmatrix}\begin{bmatrix} \vdots \\ c_{N,n_N-1} \\ c_{N,n_N} \end{bmatrix} - \begin{bmatrix} \vdots \\ \boldsymbol{y} \\ \boldsymbol{y}+K_NP_NC_{b,N} \end{bmatrix}$$

and these fluxes are specified by the given outer boundary conditions (7). Thus, we are left with a system of equations, of size $\sum_{\alpha=1}^{N}(n_\alpha + 1)$, of the form

$$\overline{\boldsymbol{M}}\frac{d}{dt}\boldsymbol{c} = \boldsymbol{A}_c\boldsymbol{c} - \boldsymbol{l}_c \tag{12}$$

where $\overline{\boldsymbol{M}}$ is a diagonal matrix, $\boldsymbol{A}_c$ is a tridiagonal matrix, the construction of which was described above, $\boldsymbol{l}$ is the load vector and $\boldsymbol{c}$ is the vector of primary state variables. Taking the secondary state variables $\boldsymbol{s}$ as given, Eq. (12) is linear.

Now, considering the secondary state of (1), we arrive at a discretization of the left hand side in a similar way as (9), whereas the right hand side discretization is derived from Eq. (10) or from a corresponding equation derived from (3) in the case of solid drug dissolution resulting in the following linear system

$$\overline{\boldsymbol{M}}\frac{d}{dt}\boldsymbol{s} = \boldsymbol{A}_s\boldsymbol{s} - \boldsymbol{l}_s \tag{13}$$

where $\boldsymbol{A}_s$ is a diagonal matrix in the two-phase case, applying mass lumping, and is empty in the drug dissolution case. Note that no flux values are involved in the secondary state so that the assembly is straight forward.

While we are restricting our attention to one-dimensional problems, we note that the same type of two step construction can be applied to finite element discretizations in higher dimensions with corresponding boundary conditions between subregions rather than layers. While the matrices $\boldsymbol{A}_c$ and $\boldsymbol{A}_s$ will remain sparse, the non-zero structure will, however, be much more complex.

Time evolution

We now set out to solve the two coupled ODE's (12) and (13) in tandem aiming to make use of the special structure of these equations in a numerically efficient and stable manner. In our timestepping algorithm we first update $\boldsymbol{s}$ values with a one-step explicit Euler scheme. We then update the $\boldsymbol{c}$ values with an implicit one-step theta method, involving the solution of (12). We then update $\boldsymbol{s}$ again, involving a similar theta method. If the maximum of the differences between the two updated $\boldsymbol{s}$ values is within a given tolerance, *tol*, we proceed to the next timestep, otherwise we repeat the calculation of the $\boldsymbol{c}$ values using updated $\boldsymbol{s}$ values, followed by a new updating of these values, and so on until a limit of *max* iterations is reached. The procedure for updating one-step thus becomes:

Note that the matrices $\overline{\boldsymbol{M}}$ and $\overline{\boldsymbol{M}} - \Delta t\theta\widetilde{\boldsymbol{A}}_s$ are diagonal so that the solution of the corresponding equations is trivial. Moreover, the matrix $\overline{\boldsymbol{M}} - \Delta t\theta\widetilde{\boldsymbol{A}}_c$ is tridiagonal so that we have an efficient algorithm also for the solution of that equation.

Other methods

While discontinuity interlayer conditions due to partition and/or mass transfer effects are presented in a number of papers on drug transport and related processes [7,12,13] the exact treatment of these conditions in simulations is rarely specified. When applying general software packages such as ANSYS, these conditions are often dealt with in some indirect way, such as adopting so-called normalized approach in ANSYS 14.5 to deal with partition. Here, great care has to be taken to avoid erroneous results, cf. eg.[14]. Similarly, in COMSOL general discontinuity interlayer conditions can only be dealt with in a roundabout way; see [15].

A general finite element approach for dealing with discontinuous interior boundary conditions within the framework of domain decomposition methods is typically based on discontinuous Galerkin finite element methods along with interior penalty functions, see e.g. [16], or on extending the finite element method by special enrichment functions (X-FEM), to account for non-smooth behaviour, see e.g. [17]. For the special type of interior boundary conditions considered in this paper it seems, however, more appropriate to incorporate them explicitly.

Rim et al. [5] did construct a finite element model for transdermal drug delivery incorporating explicitly the effects of partitioning between layers, by decomposing a partition interface into two adjacant boundaries, each belonging to separate layers as is done in our approach above. The method employed to incorporate this condition is, however, a mixed method whereby cross boundary normal flux is modeled as independant variables, in addition to the concentrations at each boundary.

Using finite differences as the numerical basis, a special difference scheme was developed by Hickson et al. [4], to deal with discontinuity in concentration between layers caused by an interlayer mass transfer condition.

Both above approaches maintain a flux continuity condition across the boundary. In our framework, all boundary effects mentioned above, including partitioning, mass transfer effects and flux continuity, are incorporated into the finite element formulation without having to introduce any additional variables or special schemes at the boundaries. This is achieved by first applying the finite element scheme separately to each layer with arbitrary flux conditions at the outer boundaries of the layer, and then assembling the layer equations into a global scheme so that flux between layers remains continuous, but also satisfies the interlayer boundary conditions.

Further note, that according to the finite element scheme we are in fact approximating $-D_\alpha \frac{\partial C_\alpha}{\partial x}\big|_{x=x_k}$ with

$$
\begin{aligned}
&= -D_\alpha \frac{c_{\alpha,k+1} - c_{\alpha,k}}{h_\alpha} - d_\alpha \frac{h_\alpha}{2} c_{\alpha,k} - \frac{h_\alpha}{2}\frac{d}{dt} c_{\alpha,k} \\
&= -D_\alpha \frac{\partial}{\partial x} c_{\alpha,k} + D_\alpha \frac{h_\alpha}{2}\frac{\partial^2}{\partial x^2} c_{\alpha,k} + O(h_\alpha^3) - \frac{h_\alpha}{2}\left(d_\alpha c_{\alpha,k} - \frac{d}{dt} c_{\alpha,k}\right) \\
&= -D_\alpha \frac{\partial}{\partial x} c_{\alpha,k} + O(h_\alpha^3)
\end{aligned}
$$

since we satisfy the differential equation at $x = x_k$. Thus, we are achieving a second order approximation without having to include $c_{\alpha,k+2}$ as is done in the second order difference scheme of [4] for the flux at an interlayer boundary.

3. Simulations

Having constructed the numerical model in 2.3, we now turn our attention to the modelling of specific cases to demonstrate its usefulness. In two cases, experimental data is used to deduce relevant pharmacokinetic processes and to quantify corresponding parameters. The data considered in this article are release curves from Franz diffusion cell (FDC) experiments whereby a test material is held in place between a drug loaded donor chamber (DC) and a receptor chamber (RC), filled with release medium; see Fig. 2. A description of the constituents of the medium and the experiment can be found in the supplement. A model describing the transport of drugs from the donor chamber, through the test material and into the receptor chamber is needed to asses the material properties; see Gudnason et al. [18].

In Section 3.1, an FDC system containing intraocular lens (IOL) material is considered, where descriptive parameters are deduced from three different thicknesses of IOLs. In 3.2, we model a transdermal system and compare the results with the semi-analytical approach of Pontrelli and de Monte [3]. In 3.3, we reconsider the transdermal experiment from Snorradottir et al. [9] and deduce descriptive parameters of skin from two separate FDC systems.

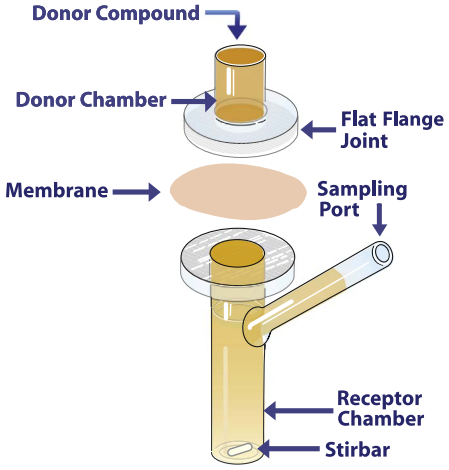

Fig. 2. Schematic depiction of Franz diffusion cell (FDC) [19]. Initially, release medium is loaded into receptor chamber (RC) and drug solution loaded into the donor chamber (DC). Drug then proceeds through the material and into the RC until equilibrium is reached. Meanwhile, samples are extracted from the RC, the concentration of which is measured. The measured concentration values form a release curve from which drug related properties of the material are inferred.

3.1. Intraocular lens simulations

Moxifloxacin loaded FDC experiments had been carried out on the intraocular lens material CI26Y by Elvar Orn Kristinsson under the supervision of Mar Masson at the Faculty of Pharmaceutical Science, University of Iceland, see supplement. The material had been provided by PhysIOL [20]. CI26Y is a hydrophilic material composed of 2-hydroxyethyl methacrylate and methylmethacrylate and has water content of 26%. The experiments were carried out on three different thicknesses of the material: 1 mm, 0.2 mm and 0.1 mm. We assume general interlayer boundary conditions at the lens boundaries with the same partition and mass transfer values between lens and liquid on both sides and that the only transport mechanism within the lens is diffusion. A schematic diagram of the model for the systems is shown in Fig. 3, which shows the diffusion equation within each layer and general boundary conditions at lens-donor and lens-receptor boundaries. The length of donor and receptor layers are 2.36 cm and 18.86 cm respectively. The different lens thicknesses were used to model the lens layer. The initial concentration drug solution in the DC is 5 mg/ml. Since stirring is applied to the receptor chamber, D_γ is set large enough to enforce instant distribution $D_\gamma = 10^5$ (cm^2/h). We also choose to set $D_\alpha = 10^5$ (cm^2/h). The IOL parameters D_β, P_l and K_l, were adjusted manually to obtain simulated release curves which fit to experimental data. Good agreement with experiments was achieved applying the same parameter values to all thicknesses; see Table 1.

The low mass transfer parameter value indicates possible interfacial resistance. In Fig. 4, we can see how simulated concentration varies with time in RC compared with experimental data. In Fig. 5, simulated values in DC are shown. Note that these values remain spatially constant through these chambers due to the high parameter values of D_α and D_γ. RC and DC concentration curves were calculated by taking the mean value within respective layers. Figs. 6–8 show concentration profiles throughout the lenses at different times.

The DC curves show that there is only a relatively small drop in DC concentration. Notable among the three RC curves is that in the case of 1 mm the RC concentration stays at zero throughout the whole duration.

More details can be obtained by analyzing the concentration profiles. In the case of 1 mm, we can see that drug levels barely rise halfway through the material, at $x = 0.5$ mm. This is caused by the low diffusion value and the relatively long travel distance.

Table 1
Fitted parameter values used for the simulation of release curves in moxifloxacin loaded FDC experiments with the IOL material CI26Y.

D_β (cm^2/h)	P_l (–)	K_l (cm/h)
$8.77 \cdot 10^{-7}$	12.65	$5.60 \cdot 10^{-5}$

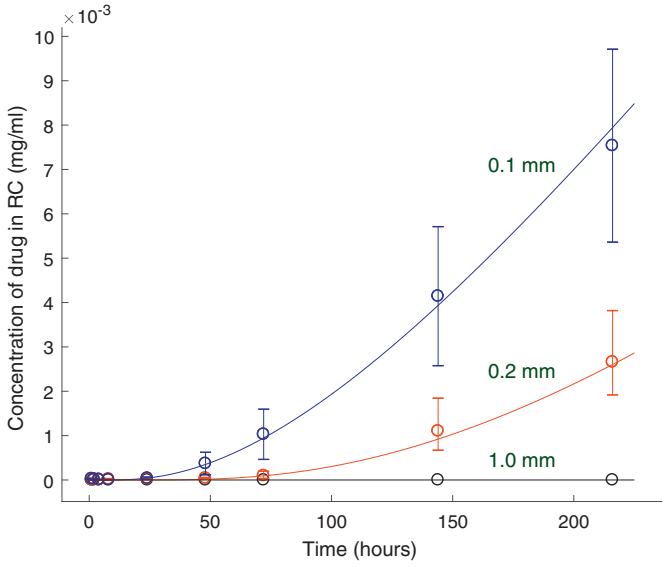

Fig. 4. Simulations of how concentration varies with time in RC in FDC experiments done on IOLs of different thicknesses. Each curve corresponds to a certain thickness. The same set of parameter values was used in each simulation; see Table 1. The vertical bars show the range of measured values in the experiments that were repeated three times. The circles show the average value from these three experiments.

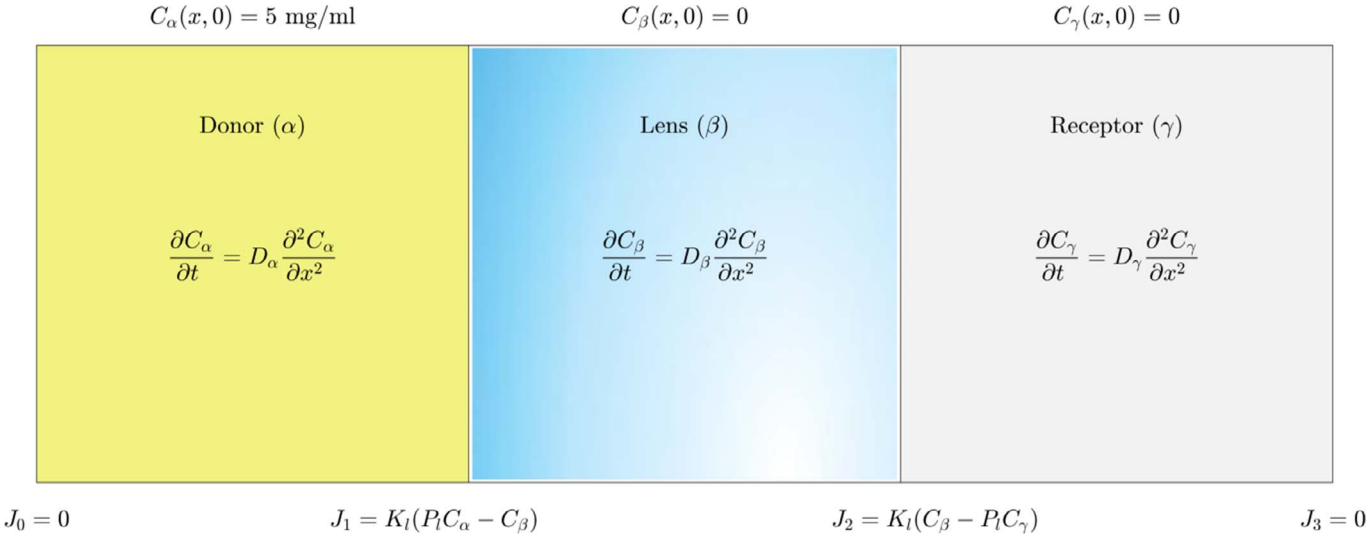

Fig. 3. A schematic model of FDC experimental systems for IOLs.

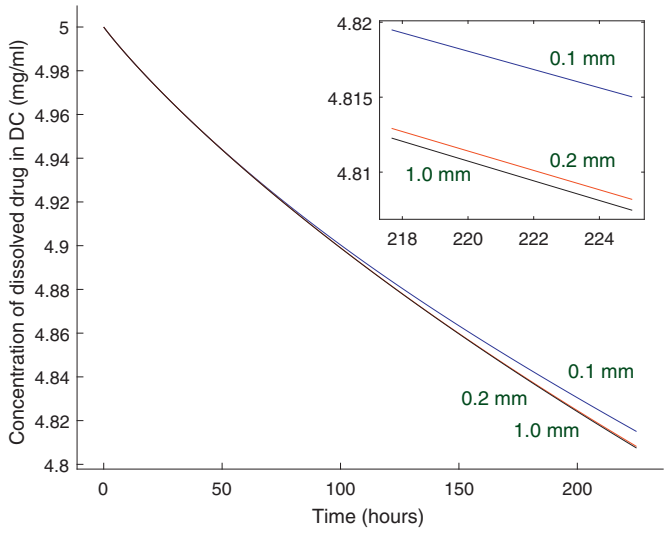

Fig. 5. Simulations of how concentration varies with time in DC in FDC experiments done on IOLs of different thicknesses. Each curve corresponds to a certain thickness.

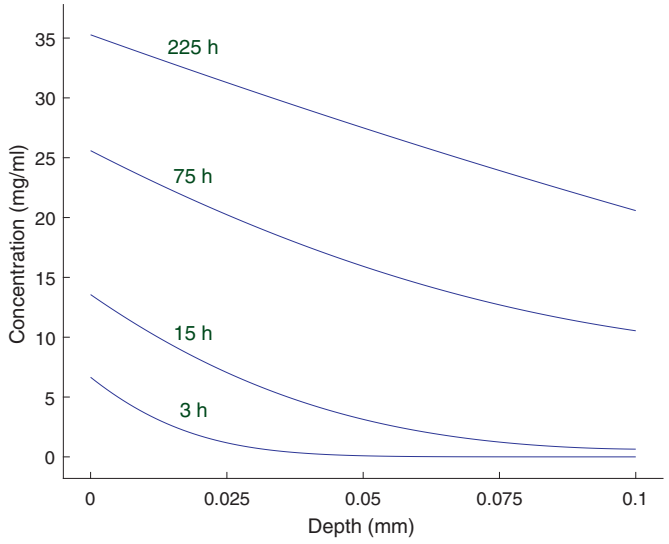

Fig. 6. Concentration profiles through 0.1 mm lens at different times.

The 0.1 mm profile at $t = 225$ h however has a constant spatial gradient whereas at the same time the profile is slightly convex for 0.2 mm. In all cases, we can observe at the DC boundary, a gradual increase of drug levels as the ratio of concentrations between lens and DC layers increases and is bounded from above by the P_l value, see Table 2. The low K_l value slows the rate at which the ratio approaches the value P_l. Finally, we note that initial attempts to obtain simulations agreeing with experiments that only involved partition effects without mass transfer effects proved unsuccessful.

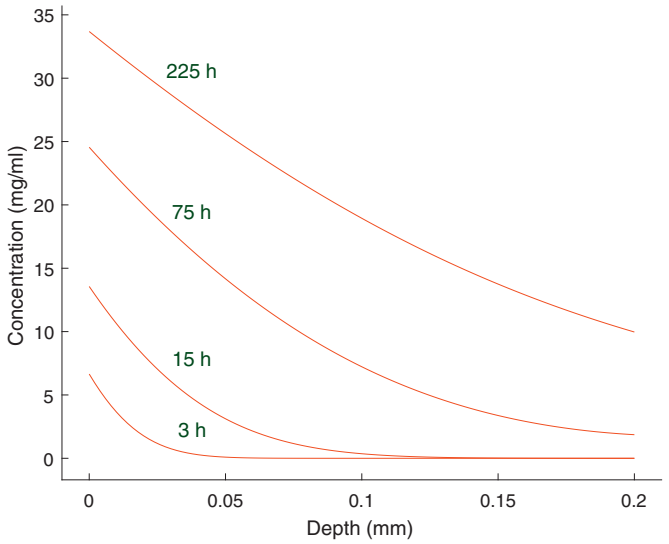

Fig. 7. Concentration profiles through 0.2 mm lens at different times.

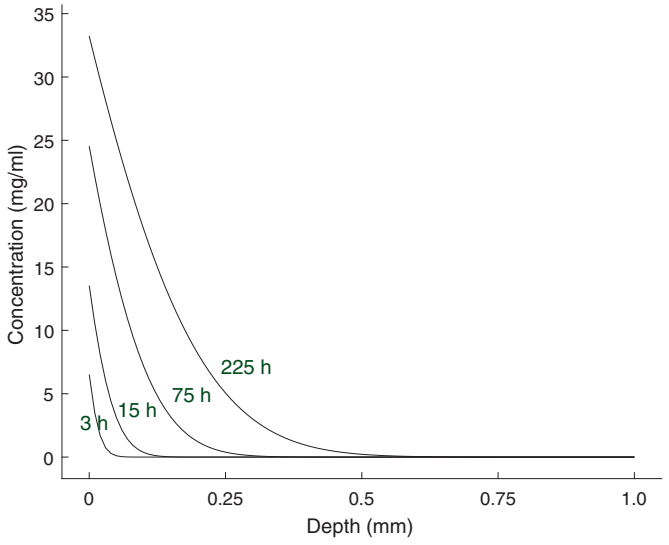

Fig. 8. Concentration profiles through 1 mm lens at different times.

Table 2
Computed discontinuity at donor-lens boundary given as ratio C_β/C_α at different times for different thicknesses of IOL.

	3 h	15 h	75 h	225 h
0.1 mm	1.3	2.7	5.2	7.3
0.2 mm	1.3	2.7	5.0	7.0
1.0 mm	1.3	2.7	5.0	6.9

3.2. Trasdermal two-phase system

In Pontrelli and de Monte [3] a two-layer transdermal drug delivery model is described with results obtained with a semi-analytical approach. The model comprises a vehicle and skin layers and describes

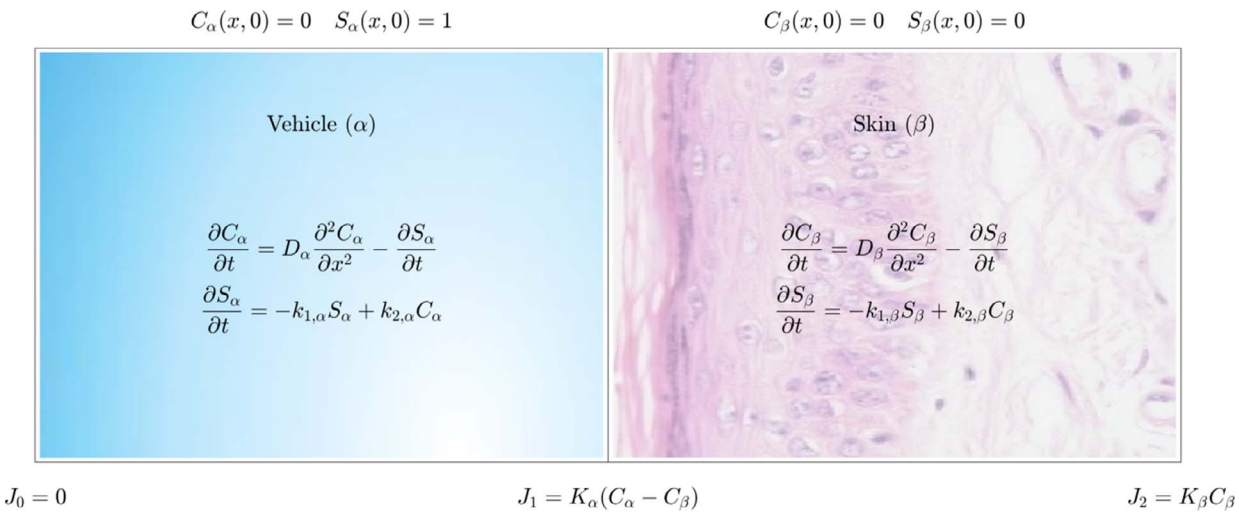

Fig. 9. A schematic model of two-phase transdermal system of [3]. Note the sink conditions on the skin outer boundary.

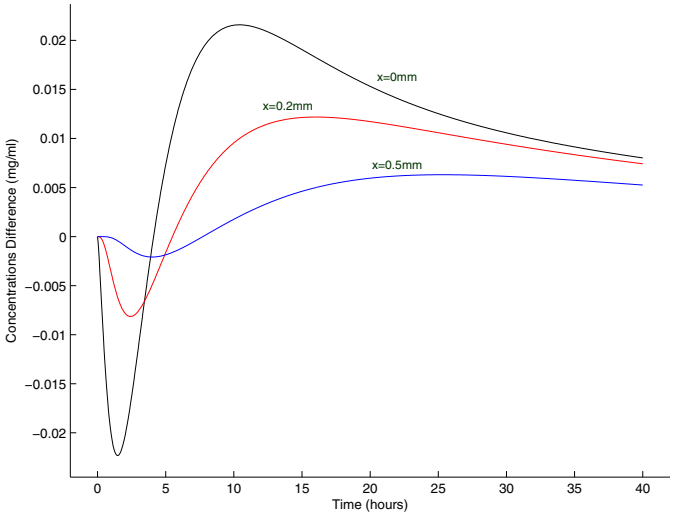

Fig. 10. Simulated curves showing time evolution of the difference of bound and unbound drug concentrations at different places within the skin layer.

diffusion and binding/unbinding within the layers, as well as, mass flux resistance between the two without partition. The mathematical schematic is shown in Fig. 9. We apply our numerical framework to this model using the same parameter values as [3]; see Table 4. We get curves which agree with those obtained by the semi-analytical approach and shown in [3]. The numerical results are presented in Figs. 10–12 and Table 4 . The main purpose of these simulations was to verify our framework in the case when the secondary state is described by the two-phase Eq. (4) since we did not have any experimental results for such a case.

In Table 4, the percentage of the two drug mass phases retained in each layer at different times are presented for the case when $k_{1,\alpha} = 0.36$, $k_{2,\alpha} = 0.36$, $k_{1,\beta} = 0.36$ and $k_{2,\beta} = 0.36$ (1/h). These results can be compared directly with results in Table 1 in [3] (Table 3).

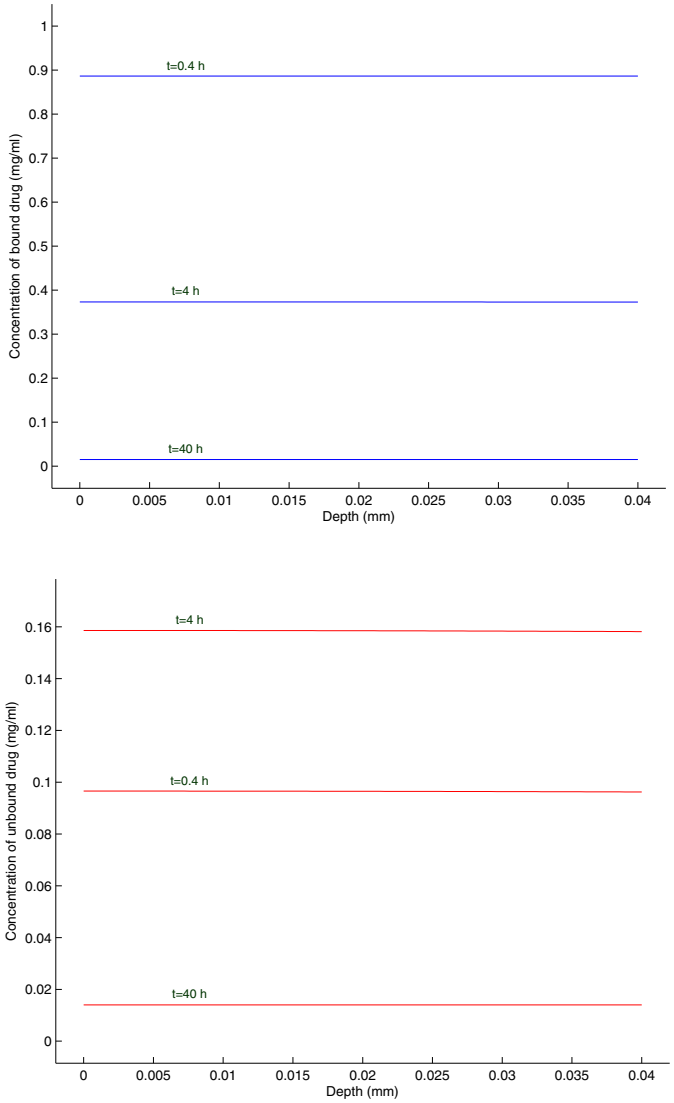

Fig. 11. Concentration profiles within vehicle layer at different times. Top: bound phase profiles. Bottom: Unbound phase profiles.

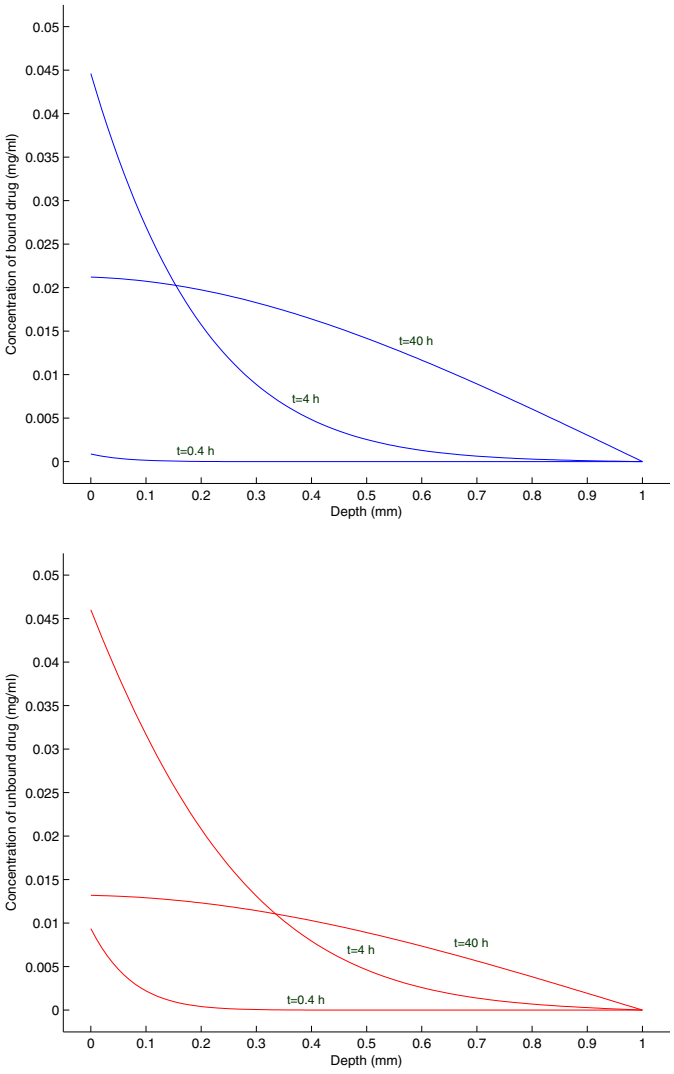

Fig. 12. Concentration profiles within skin layer at different times. Top: bound phase profiles. Bottom: Unbound phase profiles.

Table 3
Parameter values used for simulation of vehicle-skin system. Top: parameters within layers. Bottom: interlayer parameters.

Layer	H (cm)	D (cm^2/h)	k_1 (1/h)	k_2 (1/h)
Vehicle	0.2	$9.3{\cdot}10^{-3}$	0.36	0.36
Skin	$5.0{\cdot}10^{-4}$	$1.3{\cdot}10^{-8}$	0.36	0.54
Boundary				K (cm/h)
Vehicle - Skin				$3.6{\cdot}10^{-3}$
Skin - Capillary				10.8

Table 4
Percentage of the two drug mass phases retained in each layer at different times. $k_{1,\alpha} = 0.36$, $k_{2,\alpha} = 0.36$, $k_{1,\beta} = 0.36$ and $k_{2,\beta} = 0.36$ (1/h). μ_e, μ_0, μ_1 and μ_b (%) refer to bound vehicle, unbound vehicle, unbound skin and bound skin drug mass retained, respectively.

t (h:m:s)	μ_e	μ_0	μ_1	μ_b
00:23:49	87.50	10.57	01.84	00.09
01:59:03	57.29	19.95	18.04	04.72
19:50:29	03.92	03.06	34.98	36.62

3.3. Skin experiments

The framework of this paper offers an extension of the mathematical model employed in Snorradottir et al. [9] in order to simulate drug diffusing through skin. The previous model did not include mass transfer at interlayer boundaries, i.e. only included partition, defined implicitly throuh c_s values. Furthermore, drug sampling in RC is now accounted for explicitly, resulting in a discontinuous drop in concentration at each sampling time.

We simulated again with the current framework two ibuprofen experiments, described in [9], which both involve drug diffusing through skin, in order to deduce the physical parameter values assumed to be the same for both experiments. We constructed a DC-Skin system model, similar to the model introduced in 3.1 and a Matrix-Skin system model, where instead of a donor chamber, a silicone matrix containing solid drug is inserted. Schematic diagrams of the models for the experimental systems are shown in Fig. 13. Silicone matrix layer parameters describe drug properties within the silicone. They include: k', the effective dissolution of the solid drug; c_s, the solubility of the dissolved drug; and D_α, the diffusion of dissolved drug. Descriptions of the preparation of the silicone matrix material can be found in [9].

As is the case in 3.1, stirring is applied to the receptor chamber and the value of D_γ is assumed to be large ($D = 10^5$ (cm^2/h)) to enforce instant distribution. The diffusion value of D_α for the DC-Skin system is also assumed to be large. The diffusion value of the skin layer D_β, as well as skin-receptor boundary parameter values P_β and K_β are assumed to be the same in both DC-Skin and Matrix-Skin models, whereas the values for P_α and K_α, are different in both models; in the DC-Skin system they reperesent the skin-DC boundary and in the Matrix-Skin system they represent the skin-matrix boundary. Values for D_β, P_β, K_β, and both cases of P_α and K_α were adjusted manually to obtain simulated release curves which fit to experimental data. Additionally, the matrix values for D_α, k' and c_s were chosen to be close to the values selected in [9]. The initial concentration of the solid drug in the matrix layer is $1.1 \cdot 10^2$ mg/ml and the initial concentration drug solution in the DC is $1.9 \cdot 10^2$ mg/ml. The thicknesses of the various layers are; skin 0.07 cm; matrix 0.2 cm; DC 1.13 cm and RC 6.78 cm.

In Fig. 14, simulations are compared to data on how concentration varies with time in RC as well as showing similar simulations for the DC curve of the DC-Skin system. Discontinuities of the simulated RC concentration are a result of sample extraction. As 0.6 ml samples were taken from the 12 ml receptor chamber, and replaced with fresh medium, the concentration within the RC was reduced in proportion to the actual concentration loss. This was done by inserting a new spatially constant RC concentration profile 5% lower than the calculated mean value at the time of sampling.

Inferred parameter values are displayed in Table 6. Layer parameter values are mostly the same as in [9] except that the solubility is slightly higher and in fact closer to the value of $4.2{\cdot}10^{-2}$ mg/ml, obtained from a direct independant measurement.

Solid and dissolved concentration profiles through the matrix for the Matrix-Skin system are presented in Fig. 15. Solid drug gradually depletes as it dissolves, diffuses and crosses over the skin boundary. The available dissolved drug in the marix at the skin boundary decreases as the closest solid drug recedes.

Concentration profiles through the skin for both systems are shown in Fig. 16. In both cases we can observe an increase of drug levels in the skin at the DC - Skin and Matrix - Skin boundaries. In Table 5, we can see that the ratio of concentration difference between DC - Skin layers gradually increases with a K_α value similar to that presented in Section 3.1. In Matrix - Skin case however, the ratio is already close to

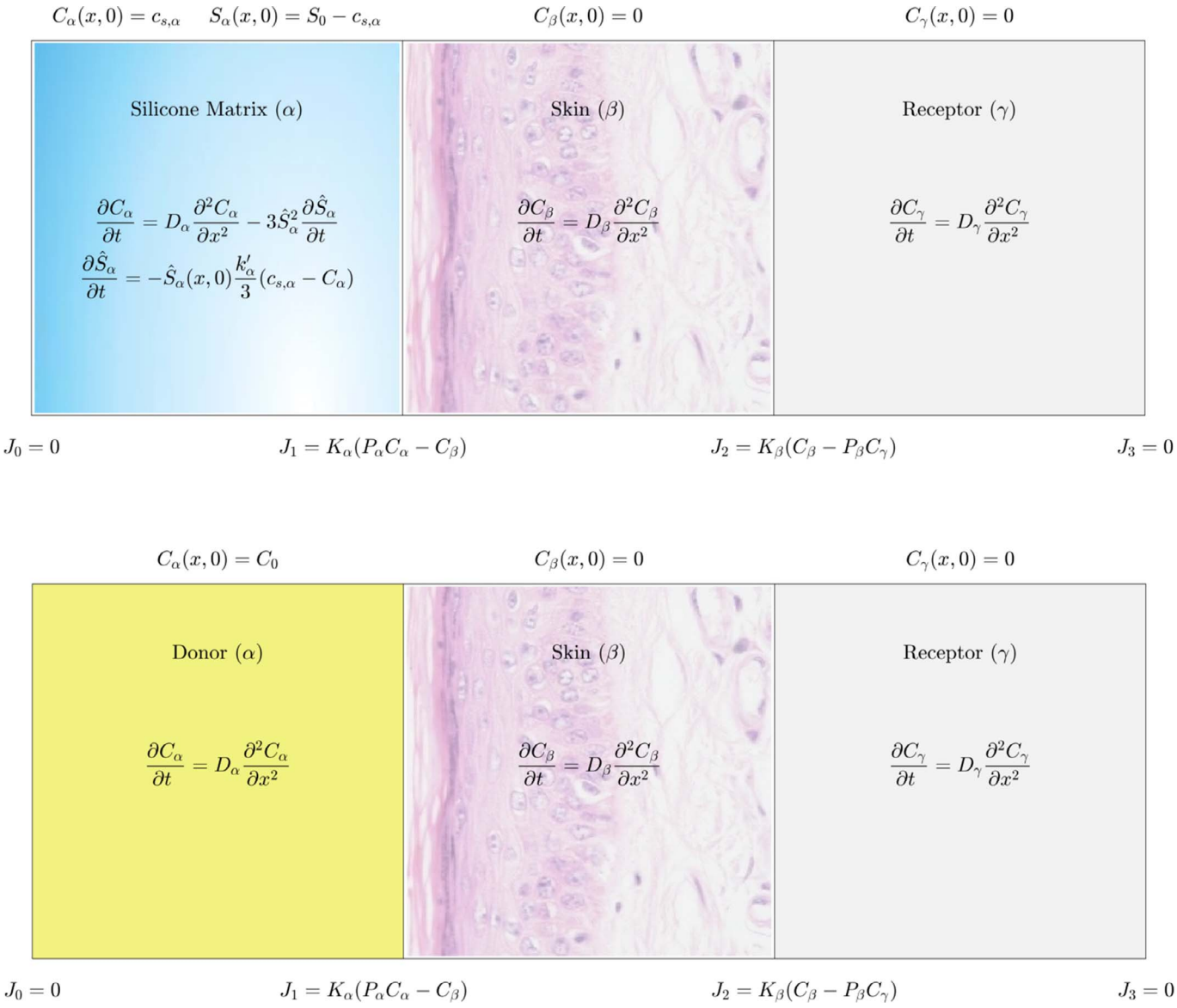

Fig. 13. Top: a schematic model of Matrix-Skin experimental system. Bottom: a schematic model of DC-Skin experimental system.

its P_α value after 1/4 h and becomes closer thereafter, in part due to the relatively high K_α value. The varying shape of the dissolved drug concentration profile within the matrix at the skin boundary also plays a role.

Donor chamber concentration change with respect to time can be seen in Fig. 17 and is held spatially the same with high D value.

The partition value between matrix and skin is more than 2 times higher and the value between donor and skin more than 50 times higher than in [9] where there was a much greater discrepancy between these two values. The corresponding mass transfer values are effectively "infinite" in [9] and thus considerably lower in the present simulations, especially between donor and skin. This could reflect the drug resistance of the epidermis, in particular that of the stratum corneum. The resulting fit is similar to that of [9] for the matrix-skin system but significantly better for the donor-skin system, indicating the importance of including both partition effects and mass transfer or barrier effects.

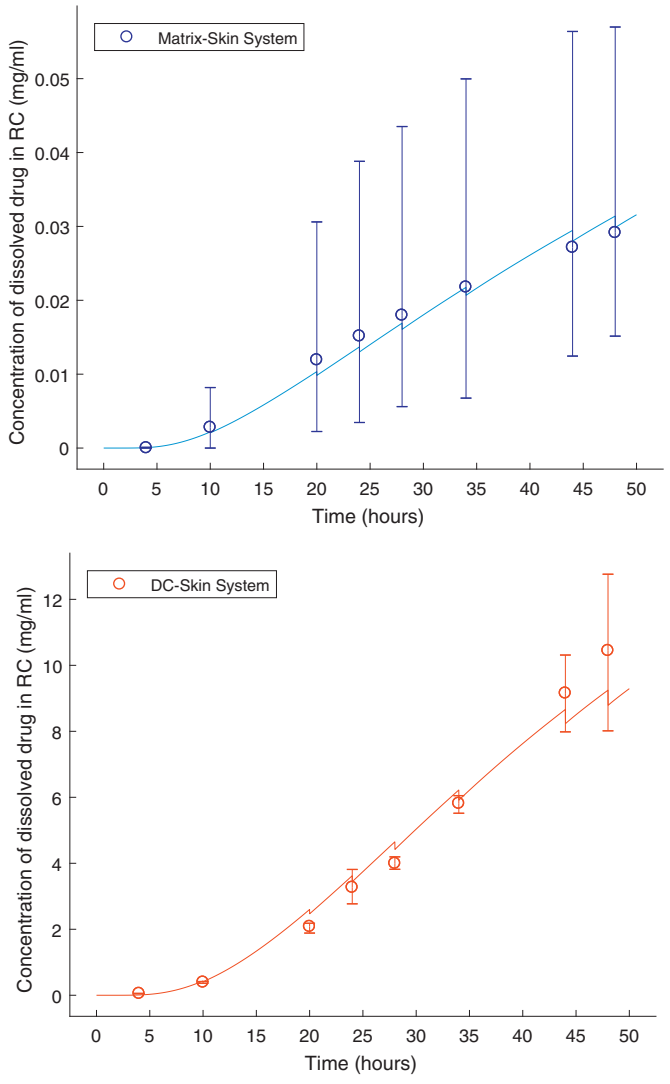

Fig. 14. Top: simulated RC curves compared with data of both systems. Curves and data have been normalized w.r.t. highest data value. Bottom: Simulated DC curve of DC-Skin system. The vertical bars show the range of measured values in the experiments that were repeated four times. The circles show the average value from these four experiments.

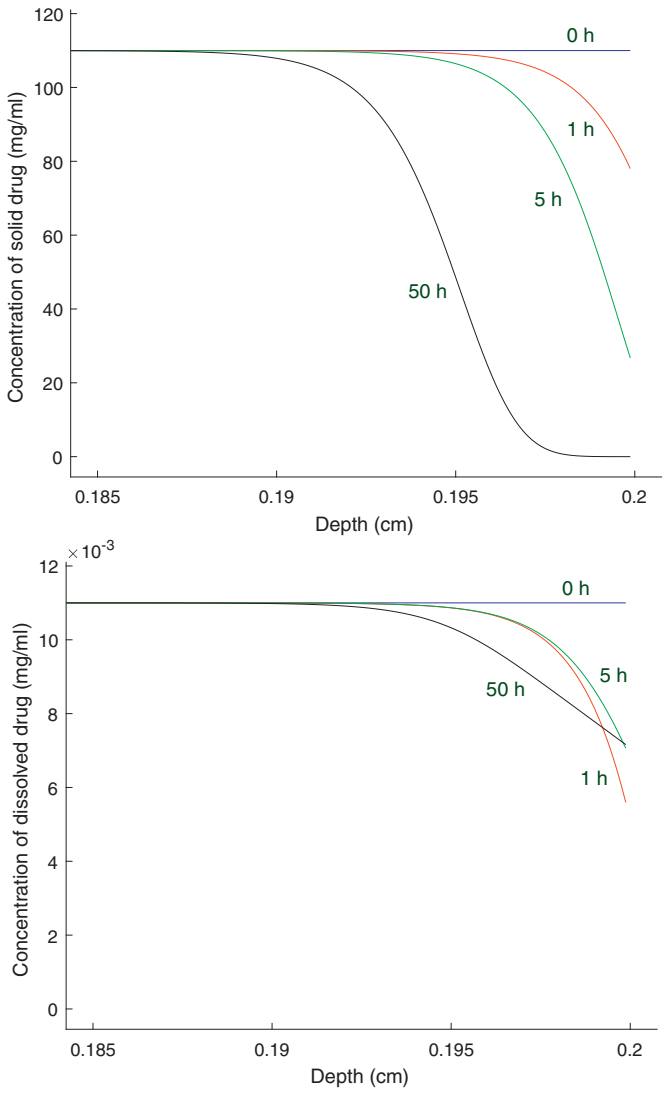

Fig. 15. Concentration profiles in silicone matrix near the skin boundary for Matrix-Skin system. Top: solid drug profiles. Bottom: Dissolved drug profiles.

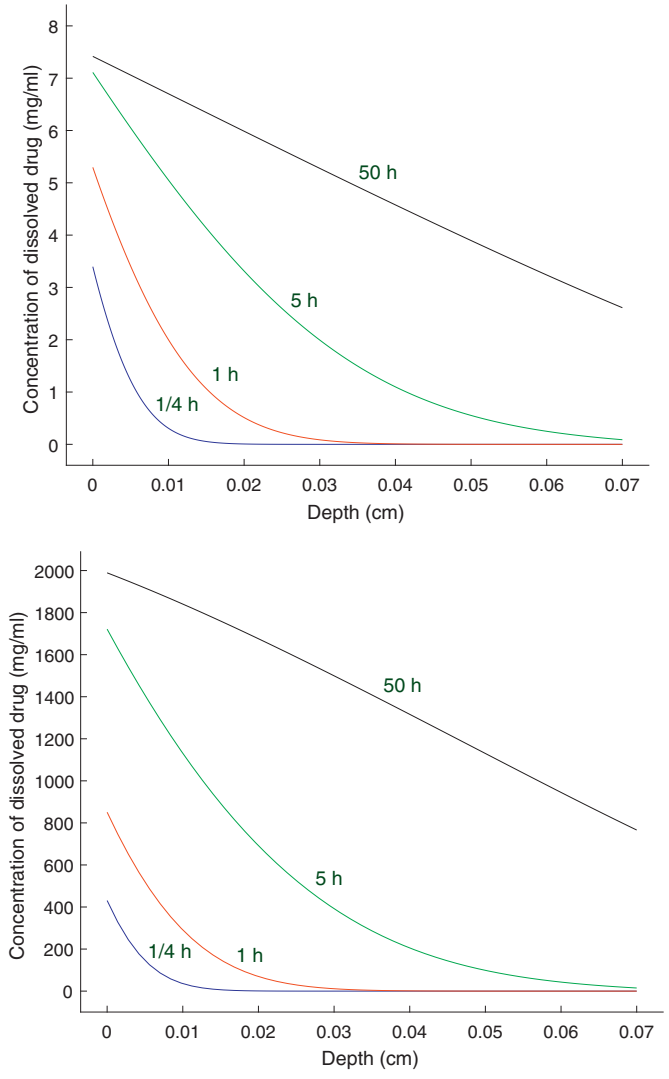

Fig. 16. Concentration profiles in skin layer. Top: Dissolved drug profiles in Matrix-Skin system. Bottom: dissolved drug profiles in DC-Skin system.

Table 5
Computed discontinuity of respective systems, at Matrix-Skin and DC-Skin boundaries, given as ratio C_β/C_α at different times.

	1/4 h	1 h	5 h	50 h
Matrix-Skin	1030	1040	1046	1049
DC-Skin	2	5	11	54

Table 6
Parameter values used for the simulation of release curves in both transdermal FDC experiments, see appropriate model schematic in Fig. 13. Top: Parameters values within layers. Bottom: Interlayer parameter values.

Layer	D (cm^2/h)	k' ($cm^3/mg\,h$)	c_s (mg/ml)
Skin	$9.3\cdot10^{-5}$		
Matrix	$9.3\cdot10^{-3}$	$5.0\cdot10^{1}$	$1.1\cdot10^{-2}$
DC	$1.0\cdot10^{5}$		
RC	$1.0\cdot10^{5}$		
Boundary		**P (−)**	**K (cm/h)**
Skin / Matrix		1050	$8.0\cdot10^{-1}$
Skin / Donor		450	$8.8\cdot10^{-5}$
Skin / PBS		70	$1.8\cdot10^{-2}$

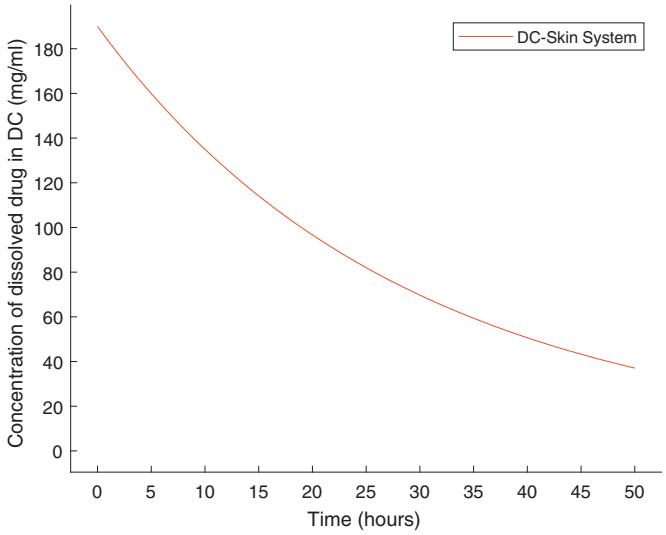

Fig. 17. Simulated DC curve of DC-Skin system.

Data: $\boldsymbol{c}_k$, $\boldsymbol{s}_k$, $\boldsymbol{A}_c$, $\boldsymbol{A}_s$, $\boldsymbol{l}_c$, $\boldsymbol{l}_s$, $\bar{\boldsymbol{M}}$, θ, max, tol
Result: $\boldsymbol{c}_{k+1}$, $\boldsymbol{s}_{k+1}$ and updated values for $\boldsymbol{A}_c$, $\boldsymbol{A}_s$, $\boldsymbol{l}_c$, $\boldsymbol{l}_s$
$k = 1$; $\varepsilon = 2\ tol$;
Solve $\bar{\boldsymbol{M}}\tilde{\boldsymbol{s}}_0 = \bar{\boldsymbol{M}}\boldsymbol{s}_k + \Delta t\,(\boldsymbol{A}_s\boldsymbol{s}_k - \boldsymbol{l}_s)$; **while** $k < max$ *and* $\varepsilon > tol$ **do**
  $\tilde{\boldsymbol{A}}_c = \boldsymbol{A}_c$ updated w.r.t $\tilde{\boldsymbol{s}}_0$; $\tilde{\boldsymbol{l}}_c = \boldsymbol{l}_c$ updated w.r.t $\tilde{\boldsymbol{s}}_0$; Solve $[\bar{\boldsymbol{M}} - \theta\Delta t\tilde{\boldsymbol{A}}_c]\boldsymbol{c}_{k+1} = \bar{\boldsymbol{M}}\boldsymbol{c}_k + (1-\theta)\Delta t(\boldsymbol{A}_c\boldsymbol{c}_k - \boldsymbol{l}_c) - \theta\Delta t\tilde{\boldsymbol{l}}_c$; $\tilde{\boldsymbol{A}}_c = \boldsymbol{A}_s$ updated w.r.t $\boldsymbol{c}_{k+1}$; $\tilde{\boldsymbol{l}}_s = \boldsymbol{l}_s$ updated w.r.t $\boldsymbol{c}_{k+1}$;
  Solve $[\bar{\boldsymbol{M}} - \theta\Delta t\tilde{\boldsymbol{A}}_s]\tilde{\boldsymbol{s}}_1 = \bar{\boldsymbol{M}}\boldsymbol{s}_k + (1-\theta)\Delta t(\boldsymbol{A}_s\boldsymbol{s}_k - \boldsymbol{l}_s) - \theta\Delta t\tilde{\boldsymbol{l}}_s$; $\varepsilon = \|\tilde{\boldsymbol{s}}_1 - \tilde{\boldsymbol{s}}_0\|$; $\tilde{\boldsymbol{s}}_0 = \tilde{\boldsymbol{s}}_1$; $k++$;
end
$\boldsymbol{s}_{k+1} = \tilde{\boldsymbol{s}}_1$; $\boldsymbol{A}_c = \tilde{\boldsymbol{A}}_c$, $\boldsymbol{l}_c = \tilde{\boldsymbol{l}}_c$, $\boldsymbol{A}_s = \tilde{\boldsymbol{A}}_s$, $\boldsymbol{l}_s = \tilde{\boldsymbol{l}}_s$.

Algorithm 1. One-step time evolution algorithm.

4. Discussion and conclusions

A numerical method was introduced to incorporate the discontinuous interlayer boundary effects of partitioning and mass transfer into the finite element scheme. The usefulness and flexibility of the framework was demonstrated with a series of models highlighting particular applications.

In 3.1, we managed to explain three release curves, corresponding to different thicknesses of IOLs, with a single set of parameter values which proved impossible without the combined effects of the partitioning and mass transfer parameters. The low mass transfer parameter value obtained in this case indicates possible surface effects which impede drug penetration and explains the lack of drug penetration for the thickest lens. In 3.2, we compared our results with those of Pontrelli and Monte when the secondary state is described by a two-phase equation. In 3.3, we looked at previously published data with an extended model including additional mass transfer parameters in order to describe a system previously modelled in [9] when the secondary state is described by a Noyes–Whitney equation. The added mass transfer parameter reflects the natural drug resistance of the skin sublayers, and improves the resulting fit.

In general published data on drug release does not describe concentration profiles thoughout the material, which limits the scope of testing the reliability of proposed models. A notable exception however can be found in [7] where a cornea is studied with the fluorescent compound rhodamine and trans-corneal concentration profiles of the compound can be directly assessed and modelled. It is of interest to note that both partition effects and mass transfer effects had to be included to simulate the measured concentration profiles.

As suggested by [21,22], mass transfer conditions, sometimes refered to as Kedem–Katchalsky conditions, can be used to model partitioning effects. In particular, the conditions can be used to model a control barrier with partition, as described in 2.2, in the case when $P_- P_+ = 1$. In more general settings however, this approach does have its limitations. Firstly, mass transfer discontinuities arise only when there is a flux. This means that for a system in equilibrium, naturally occuring jumps in concentration cannot be adequately modelled. Secondly, mass transfer conditions can only describe negative jumps in the direction of the flux. In some cases however, a positive jump can occur as in 3.1 and 3.3 see also e.g. [7,23].

Acknowledgments

We thank financial support from the Technical Development Fund of Rannís (grant no. 13-1309) as part of jointly funded European M-Era-Net project SurfLenses (M-ERA.NET/0005/2012).

We would like to thank Dimitriya Bozukova and PhysIOL [20] for supplying the intraocular lens material used in 3.1 and Elvar Orn Kristinsson for conducting the intraocular lens Franz Diffusion experiments.

References

[1] G. Frenning, Theoretical investigation of drug release from planar matrix systems: effects of a finite dissolution rate, J. Controlled Release 92 (3) (2003) 331–339.
[2] G. Frenning, U. Brohede, M. Strømme, Finite element analysis of the release of slowly dissolving drugs from cylindrical matrix systems, J. Controlled Release 107 (2) (2005) 320–329.
[3] G. Pontrelli, F. de Monte, A two-phase two-layer model for transdermal drug delivery and percutaneous absorption, Math. Biosci. 257 (2014) 96–103.
[4] R. Hickson, S.I. Barry, G.N. Mercer, H. Sidhu, Finite difference schemes for multilayer diffusion, Math. Comput. Model. 54 (1) (2011) 210–220.
[5] J.E. Rim, P.M. Pinsky, W.W. van Osdol, Finite element modeling of coupled diffusion with partitioning in transdermal drug delivery, Ann. Biomed. Eng. 33 (10) (2005) 1422–1438.
[6] S. McGinty, G. Pontrelli, A general model of coupled drug release and tissue absorption for drug delivery devices, J. Controlled Release 217 (2015) 327–336.
[7] C. Gupta, A. Chauhan, R. Mutharasan, S.P. Srinivas, Measurement and modeling of diffusion kinetics of a lipophilic molecule across rabbit cornea, Pharm. Res. 27 (4) (2010) 699–711.
[8] A. Pimenta, J. Ascenso, J. Fernandes, R. Colaço, A. Serro, B. Saramago, Controlled drug release from hydrogels for contact lenses: drug partitioning and diffusion, Int. J. Pharm. 515 (1) (2016) 467–475.
[9] B.S. Snorradottir, F. Jonsdottir, S.T. Sigurdsson, M. Masson, Numerical modelling of transdermal delivery from matrix systems: parametric study and experimental validation with silicone matrices, J. Pharm. Sci. 103 (8) (2014) 2366–2375.
[10] A.A. Noyes, W.R. Whitney, Drug dissolution, J. Am. Chem. Soc. 19 (1897) 930–934.
[11] B.S. Snorradóttir, F. Jónsdóttir, S.T. Sigurdsson, F. Thorsteinsson, M. Másson, Numerical modelling and experimental investigation of drug release from layered silicone matrix systems, Eur. J. Pharm. Sci. 49 (4) (2013) 671–678.
[12] S. Gause, K.-H. Hsu, C. Shafor, P. Dixon, K.C. Powell, A. Chauhan, Mechanistic modeling of ophthalmic drug delivery to the anterior chamber by eye drops and contact lenses, Adv. Colloid Interface Sci. 233 (2016) 139–154.
[13] S. Becker, A. Kuznetsov, Heat Transfer and Fluid Flow in Biological Processes, Academic Press, 2014.
[14] D. Liu, S. Park, A note on the normalized approach to simulating moisture diffusion in a multimaterial system under transient thermal conditions using ansys 14 and 14.5, J. Electron. Packag. 136 (3) (2014) 034501.
[15] A. Datta, V. Rakesh, An Introduction to Modeling of Transport Processes: Applications to Biomedical Systems (p.372), Cambridge University Press, 2010.
[16] A. Cangiani, E.H. Georgoulis, M. Jensen, Discontinuous galerkin methods for convection-diffusion problems modelling mass-transfer through semipermeable membranes, Proceedings of the Congress on Numerical Methods in Engineering, Coimbra, (2011).
[17] J. V., G. C., B.R. Akula, V.A. Yastrebov, Domain tying across virtual interfaces: coupling X-FEM with the mortar method, CSMA 2017: 13e colloque national en calcul des structures, Giens, France, (2017).
[18] K. Gudnason, S. Solodova, A. Vilardell, M. Masson, S.T. Sigurdsson, F. Jonsdottir, Numerical simulation of franz diffusion experiment: application to drug loaded soft contact lenses, J. Drug Delivery Sci. Technol. (2017).
[19] PermeGear. URL http://permegear.com/.
[20] PhysIOL. URL http://www.physiol.eu.
[21] S. McGinty, D. King, G. Pontrelli, Mathematical modelling of variable porosity coatings for controlled drug release, arXiv preprint arXiv:1701.04989 (2017).
[22] J. Ferreira, P. de Oliveira, P. da Silva, R. Silva, Mathematics of aging: diseases of the posterior segment of the eye, Comput. Math. Appl. 73 (1) (2017) 11–26.
[23] H. Okamoto, F. Yamashita, K. Saito, M. Hashida, Analysis of drug penetration through the skin by the two-layer skin mode, Pharm. Res. 6 (11) (1989) 931–937.